Arid Zone Journal of Engineering, Technology and Environment, February, 2017; Vol. 13 (1): 149-162

Print ISSN: 1596-2490, Electronic ISSN: 2545-5818, www.azojete.com.ng

NUMERICAL PREDICTIONS OF ENHANCED IMPINGEMENT JET COOLING WITH RIBS AND PINS IN CO-FLOW AND CROSS-FLOW CONFIGURATIONS

A. M. El-Jummah[*1], F. A. Oluwole[1], G. E. Andrews[2] and J. E. J. Staggs[2]

[1]*Department of Mechanical Engineering, Faculty of Engineering, University of Maiduguri, Nigeria.*
[2]*Energy Research Institute, School of Chemical and Process Engineering, University of Leeds, LS2 9JT, UK*

**Corresponding Author's e-mail address: al-jummah@hotmail.com, GSM: +234(0)8037803678*

Abstract

Numerical calculations relevant to gas turbine internal wall heat transfer cooling were conducted using conjugate heat transfer (CHT) computational Fluid Dynamics (CFD) commercial codes. The CHT CFD predictions were carried out for impingement heat transfer with different types of obstacle walls (fins) on the target surfaces. A 10 × 10 row of impingement air jet holes (or hole density *n* of 4306 m^{-2}) was used, which gives ten rows of holes in the cross-flow direction and only one heat transfer enhancement obstacle per impingement jet was investigated. Previously, four different shaped obstacles were investigated experimentally and were used to validate the present predictions. The obstacle walls, which were equally spaced on the centreline between each impingement jet are of the co-flow and cross-flow configurations. The impingement jet pitch X to diameter D, X/D and gap Z to diameter, Z/D ratios were kept constant at 4.66 and 3.06 for X, Z and D of 15.24, 10.00 and 3.27 mm, respectively. The obstacles investigated were ribs and rectangular pin-fins shapes, using two obstacles height H to diameter, H/D ratio of 1.38 and 2.45. Computations were carried out for three different mass flux G of 1.08, 1.48 and 1.94 kg/sm^2. Relative pressure loss ΔP/P and surface average heat transfer coefficient (HTC) *h* predictions for the range of G, showed good agreement with the experimental results. The prediction also reveals that obstacles not only increases the turbulent flows, but also takes away most of the cooling heat transfer that produces the regions with highest thermal gradients. It also reduces the impingement gap downstream cross-flow.

Keywords: Numerical, internal wall, conjugate heat transfer, jet cooling, pins, thermal gradients

1. Introduction

Advances in gas turbine (GT) cooling technologies require that impingement jet heat transfer system is also optimized for effective wall cooling. The impingement air jet cooling systems normally enables the air mass flow to be minimized, which is usually without effusion film cooling, but there is an influence of cross-flow in the impingement gap (Andrews and Hussain, 1984, Bunker, 2008, El-Jummah *et al.*, 2014b, 2016, Friedman and Mueller, 1951, Kercher and Tabakoff, 1970, Tapinlis *et al.*, 2014). This cross-flow showed that the impingement air from the first rows of jets flows along the gap to the trailing edge exit (Andrews and Hussain, 1987). This has been found to reduce the surface heat transfer in the downstream portion of the cooled surface, which has also been predicted by El-Jummah *et al.* (2014b, 2013a, 2013b, c) using 3D CHT CFD. This is a greater problem in wall cooling design for GT combustor walls as the distances to be cooled are greater than in turbine blades. However, the reasons for this deterioration in heat transfer that are often simply ascribed to the deflection of the impingement jet by the cross-flow are not well understood. CFD investigations of the aerodynamics in the impingement gap showed that the effect of cross-flow is more complex. Its movement is linked to the impingement jet turbulence that covers only the downstream portion of the jet. This also affects the deflection of the reverse flow jet that reduces the efficient removal of heat, from the cooled surface and increases the heat transfer to the impingement jet surface. Andrews *et al.* (2003, 2006) experimentally, used the test rig of Figure 1 (i) and the test walls of Figure 1 (ii), as typical obstacle walls (fins) to investigate these effects and also augment the impingement cooling heat transfer of gas turbine hot walls. The present CHT CFD work, investigates their experimental results for the ribs and pins in co- and cross-flows alignments.

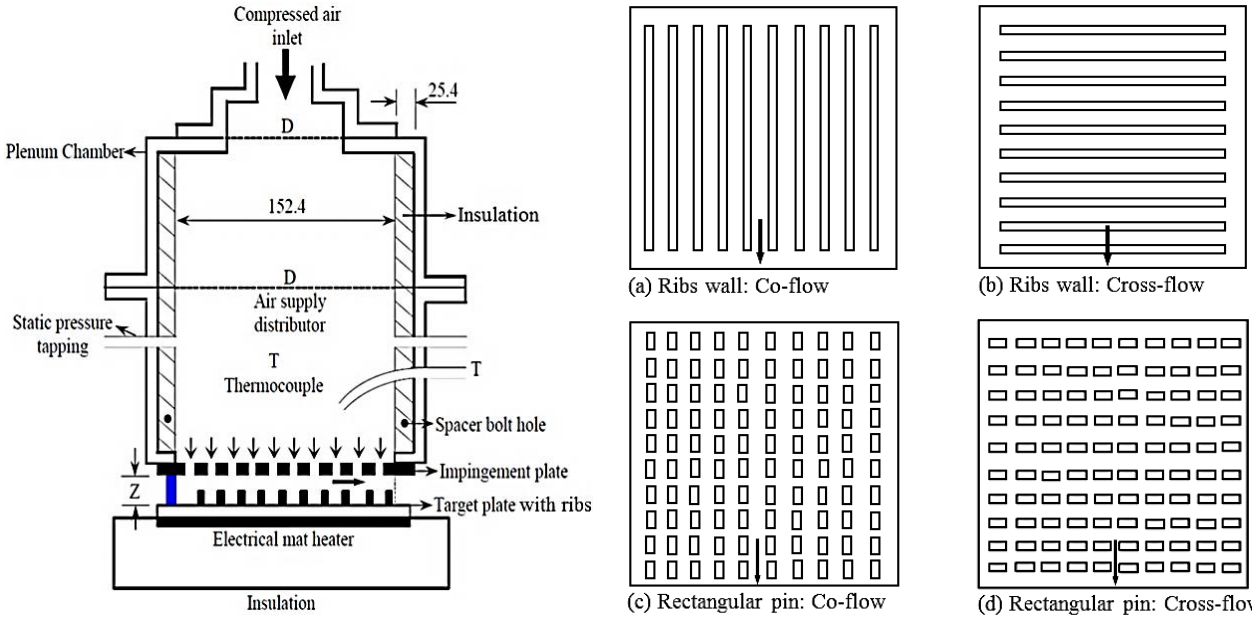

(i) Experimental test rig (ii) Experimental obstacles target plates

Figure 1: Impingement Heat Transfer cooling experimental rig and test walls schematic diagrams

1.1 Review on Impingement Heat Transfer Enhancement

The use of obstacles as flow turbulators have been shown to augment heat transfer in GT cooling channels and the typically used obstacles are the ribs wall, rectangular pin, dimples, pin-fins or cylindrical pins, bumps and perforated ribs. However the literature on the addition of various turbulators in the impingement gap, shows that enhancing the already high impingement heat transfer is quite difficult and a 20 % increased would be a good optimization. Andrews *et al.* (2003), Abdul Husain and Andrews (1991), Trabold and Obot (1987), Spring *et al.* (2012) and Taslim and Fong (2011) have experimentally investigated ribs walls at 90^{o} with the impingement jet flows across the ribs. Spring *et al.* (2012) investigation was with the application of CFD using SST model, the predictions were to near 10 % agreement with their experimental average *h* and with over 50 % local *h*, but with test wall differences for the two conditions. The results for their in-lined ribs arrangement showed heat transfer degradation due to increased cross-flow effects, while for the staggered arrangement 20 - 50 % enhancement downstream from row 5 was recorded. Trabold and Obot (1987) investigated ribbed wall cross-flow for two jet exit flows and found better enhancement for the maximum scheme exit flows. They showed heat transfer degradation at the upstream due to induced cross-flow and downstream enhancement based on X/D effects. Taslim *et al.* (2001) combined radial ribs with bumps for combined impingement jet and film cooling, enhancement due to the bumps in the presence of film cooling holes was shown. They also showed 65 % enhancement *h* in the present of showerhead film cooling holes and 35 % enhancement, for only the conical bumps and without film holes. Hoefler *et al.* (2012) investigated ribbed surfaces using staggered oblique impingement jets that were inclined with the ribs aligned to the jets, enhancement from 12 - 27 % were recorded at 25 % surface increment. Impingement heat transfer enhancements have also been used on heated cubes, using numerical approach for varied Reynolds number Re (Rundstrom and Moshfegh, 2008), flow aerodynamics were predicted from the analysis.

The used of ribbed walls have also been applied by several authors to gas turbine cooling applications. Wang *et al.* (1998) investigation was using inclined ribs configurations in a film cooling system, whereby flow and thermal fields were predicted using 2D CFD. Chung et al. (2014) investigated inclined ribs that intersected in a duct for internal cooling of GT turbine blades. Andrews *et al.* (2003) investigated ribs parallel to the impingement jet cross-flow that gave a small increment in heat transfer, as compared to smooth surface. In the downstream section of the cross-flow duct, the enhancement at low G was as high as 30 % for the best rib geometry. But for the surface averaged heat transfer, this was only 10 - 20 % enhancement at low G and no enhancement at high G. They found that there was an improved enhancement if the ribs were slotted and of greater height relative to the duct, this gave a rectangular pin geometry, which is modelled in the present work. Shizuya and Kawaike (1987) investigated a wide range of enhanced impingement cooling configurations, the most effective was a 50 % improvement in heat transfer using cylindrical pin-fins in a square array as compared to a smooth wall. Azad *et al.* (2002) also investigated impingement jet cooling heat transfer enhancement using pin-fins for a 4 × 12 holes for three coolant mass flows and with five pins serving each jet flow. A recent development in enhanced heat transfer is the application of dimple obstacles in the target surface, Xie *et al.* (2013) studied three different dimple obstacles configurations and found that the optimum heat transfer was for a dimple depth δ to its diameter D_o, ratio δ/D_o of 0.3, which was the largest investigated. Ligrani *et al.* (2003) and Ligrani (2013) reviewed heat transfer enhancement as applied to internal cooling of turbine components, they concluded that ribbed wall obstacles gave a higher heat transfer enhancement.

1.2 The Test Walls Previous Experimental Procedure

The experimental techniques have been fully detailed by previous investigators, the test rig shown in Figure 1 (i), have been used experimentally as stated above, in investigating the enhanced impingement heat transfer. This was for two types of obstacles (fins): ribs and rectangular pins, with two cross-flow alignments of co- and cross-flow as in Figure 1 (iia - d). The pins obstacle heights were higher than for ribs and both were designed to have the same total fin area. The test walls had ribs machined from a solid block of stainless steel. The rectangular pins or slotted ribs were intended to generate more turbulence in channel flow or co-flow as seen in Figure 1 (iia and c) and large scale recirculation and enhanced turbulence in cross-flow as in Figure 1 (iib and d).

The co-flow arrangement of the obstacle walls, gave low blockage of 5.8 % for ribs and 10.4 % for the rectangular pin-fins to the flow, hence would have a low enhancement of the pressure loss. While the rib transverse to the cross-flow with 50 % of the total cross-flow area blocked and 80 % for the rectangular pin. The aim was to utilise the internal impingement jet recirculating flow in the gap and the cross-flow to scrub the fins and enhance the heat removed from the wall. The main design aim was to utilise additional surface area for heat transfer and to use the rectangular pin-fins to investigate whether the turbulence generated was beneficial relative to the increase in pressure loss that would occur. Experimentally, the heat transfer surface area was taken as the same as that of the smooth wall by ignoring the increase in surface area due to the obstacle walls. Currently, this experimental procedure could likely affect the predictions, as the exact methods followed in removing the obstacle wall may also include in the CHT CFD the heated portion of the solid therein.

2. CFD Methodology

2.1 Model Grid Geometry

The geometries modelled in this work, have the same configuration with the smooth impingement target wall geometries that were used for single exit cooling experimental investigation. Table 1 summarised the 10 × 10 array of impingement jet holes (El-Jummah, 2014a, b, 2013a) geometry that was tested, for varied coolant mass flux G from 1.08 - 1.93 kg/sm^2. The smooth wall results have been predicted by El-jummah *et al.* (2013a) with good agreement with the experimental surface average HTC and the gap exit pressure loss. This work investigates using the same geometrical configurations as Figure 2 (i) show, the potential improvement in the heat transfer using obstacle walls on the target surface, as in Figure 1 (ii) with dimensions in Table 2 and Figure 2 (ii). The obstacle walls were those investigated by Andrews et al. (2003, 2006) and Abdul Hussain and Andrews (1991) with a fin thickness t, of 3 mm, as shown in Figure 2 (iia). The ribs consisted of a continuous rib of height H that was 45 % of Z as in Figure 2 (iia) or rectangular pin with H as 80 % of Z as in 2 (iib or c) with equal pin width W and pin gap. These two obstacles were investigated for two cross-flow directions relative to the fins: co-flow parallel to the fins and cross-flow which is across. Figure 3 show the symmetrical elements of the control volumes that were used in modelling the model grids geometries of Figure 4, 3a for the ribs wall in cross-flow and 3b for rectangular pin in co-flow. The blockage of the obstacles was greater in the cross-flow direction and so the pressure loss increased was higher.

Table 1: Geometric Variables

Variables	Dimensions
D (mm)	3.27
X (mm)	15.24
Z (mm)	10.0
L (mm)	6.35
L/D	1.94
X/D	4.66
Z/D	3.06
X/Z	1.52
n	4306 m^{-2}
Array	10 × 10

Table 2: Obstacle Walls Parameters

Types	W (mm)	H (mm)	t (mm)	H/W
RW: co-flow	continuous	8.00	3.0	
RW: cross-flow	continuous	8.00	3.0	
RP: co-flow	8.59	4.50	3.0	0.93
RP: cross-flow	8.59	4.50	3.0	0.93

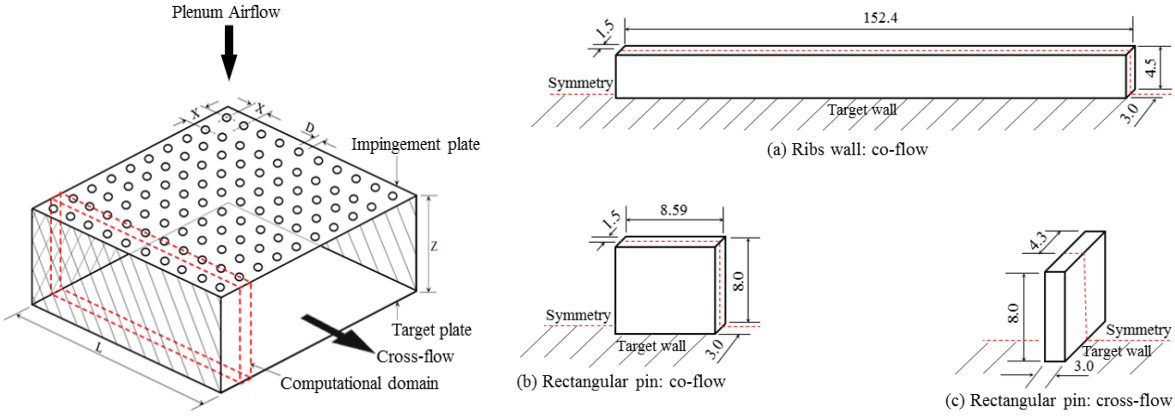

(i) Geometrical setup and flow scheme (ii) Cross-section and dimensions of the obstacles

Figure 2: The 3D symmetrical elements of the model geometry

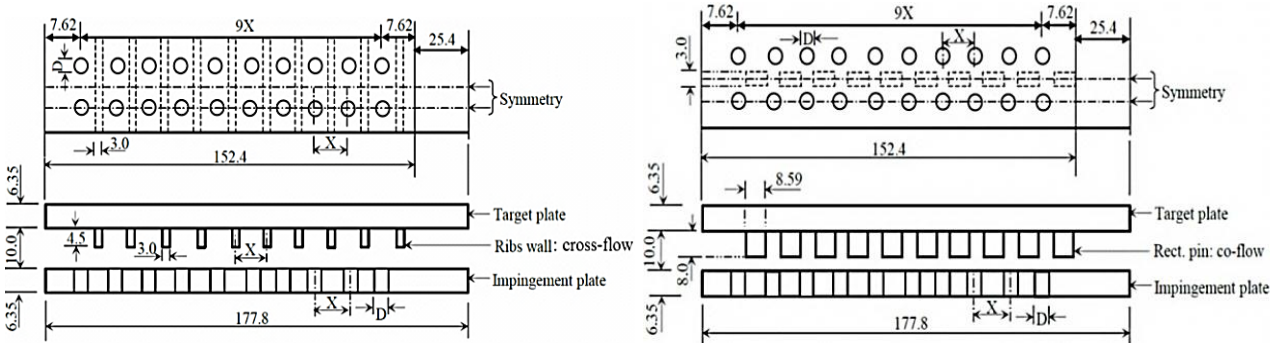

(a) Ribs wall: cross-flow (b) Rectangular pin: co-flow

Figure 3: Symmetrical elements of the computational domains

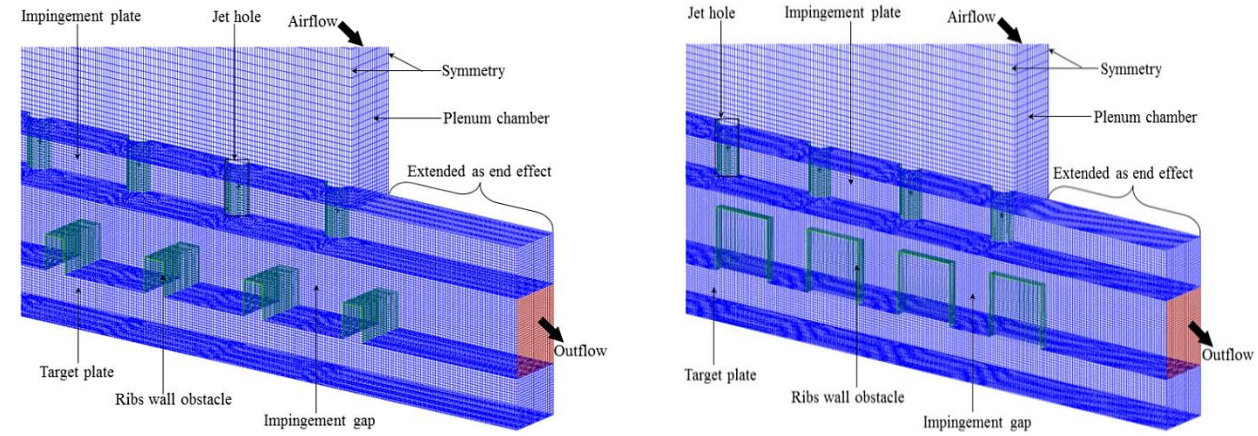

(a) Ribs wall: cross-flow model geometry (b) Rectangular pin: co-flow model geometry

Figure 4: Grid model geometries with the obstacle walls on target surface

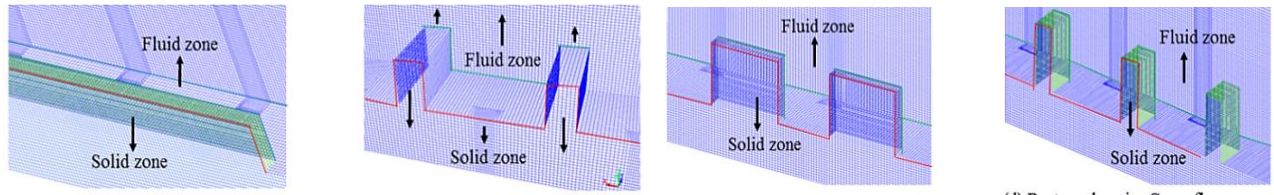

(a) Ribs wall: Co-flow (b) Ribs wall: Cross-flow (c) Rectangular pin: Co-flow (d) Rectangular pin: Cross-flow

Figure 5: The model grids of the obstacle walls on the impingement target surface

The gap between the top of the rectangular pin is necessary to allow for thermal expansion as the wall and rib are hotter than the impingement wall. If there was a solid connection, differential thermal expansion would create thermal stresses and cracking. Figure 4 (a and b) show the hexahedral computational grid that was modelled using the symmetrical representation of Figure 3 (a and b), which are one row of impingement half holes that were generated using ANSYS ICEM meshing tool for y^+ ~35 as Table 3 show. For each obstacle arrangement and for each G, as in Figure 5 (a - d) and as Table 4 show, an entirely new model grid geometry has to be modelled in order to achieve a successful computation. The obstacles in co-flow were modelled on the symmetry plane between holes, which involved half the obstacle width, while the cross-flow obstacles were modelled using the whole obstacle width. For all the obstacle grid model geometries, a minimum total cells size of 1.35×10^6 for the low G and ~1.45×10^6 maximum for the highest G were modelled, Table 3 show the parts percentage grids.

Table 3 Percentage of Parts Grids for y^+ ~35

Types	Parts (%)			
	Test walls	Obstacles	Gap	Holes
RW: co-flow	28.5	8.1	19.7	8.4
RW: cross-flow	28.5	8.1	19.7	8.4
RP: co-flow	28.5	7.2	20.6	8.4
RP: cross-flow	28.5	7.2	20.6	8.4

Table 4 Flow Conditions

G (kg/sm^2)	1.93	1.48	1.08
V_j (m/s)	43.41	33.5	24.3
U_c (m/s)	24.0	18.4	13.4
V_j/U_c	1.8	1.8	1.8
Re_h	9680	7440	5400
T_∞(K)	288	288	288
T_w (K)	353	353	353
ρ (kg/m^3)	1.225	1.225	1.225

2.2 Model Computation and Procedures

Bailey and Bunker (2002) and Spring *et al.* (2012) applied a low Re turbulence model (SST) and predicted the locally HTC *h* on the target plates, El-jummah *et al.* (2014a, b) applied high Reynolds Re (= $\rho V_j D/\mu$) model in predicting their available locally surface average *h* and aerodynamics, while Shariff and Mothe (2009, 2010) predicted locally *h* with low and aerodynamics with high Re models. Bailey and Bunker (2002) also used high Re in predicting the aerodynamics pressure loss. El-jummah *et al.* (2014a, b, 2013a) predicted cases of wall conductive heat transfer for conditions were Biot numbers < 0.2, using a high Re standard k - ε turbulence model, which this work is also employing. This CHT CFD incorporates both fluid and solid zones as in Figure 5 using the high Re turbulence model already validated. This is because the flow aerodynamics in the impingement gap is a major aspect of the flow and these includes strong flow recirculation, which the k - ε model has shown good predictions.

The obstacle walls model grids were computed for varied G of 1.08, 1.48 and 1.98 kg/sm^2, respectively using ANSYS Fluent solver with a wall function y^+ value ~35 as in Table 3. These y^+ values have been reported to be in the range $30 < y^+ < 300$ of the near wall law of the wall values. Table 4 show the model computational flow conditions that were used and are those used by El-jummah *et al.* (2013a). The convergence criteria were set at 10^{-5} for continuity, 10^{-11} for energy and 10^{-6} for k, ε and momentum (x, y and z velocities), respectively. The minimum orthogonal quality and aspect ratio, for all the geometries modelled were fixed at 0.61 and 3.53, respectively. The number of cells in all computational zones have been shown to be adequate based on grid sensitivity tests by El-jummah *et al.* (2013b, c). Typical of these cell zones are in the holes, where flow separation and reattachment dominates, impingement gap duct flow where the exit pressure loss and target surface heat transfer are most significant and the test walls where the thermal gradients prevails. Second-order discretization for momentum and first-order discretization, for TKE and dissipation of TKE using the PISO schemes based on PRESTO have been employed.

3. Computational Results

3.1 Influence of Aerodynamics on the Velocity Profiles

The aerodynamics in the impingement gap is complex, as was predicted by El-jummah *et al.* (2015, 2016, 2013b) using CHT CFD modelling. The additions of obstacles to the target wall was aimed at increasing the heat transfer by inserting the obstacles at the location of the reverse flow between each impingement jet. This increases the complexities of the aerodynamics as the cross-flow builds up with succesive rows of impingement jets. Figures 6 (ia - d) show the flow velocity profiles for all the obstacle geometries, which are for the symmetry planes of the jet holes. Figures 6 (i) clearly show that the flow-maldistribution (predicted velocity in the hole normalized to the mean using

Equation 1) between the holes that were presented in Figure 6 (ii), are the influence of the peak velocity scales in the downstream holes. The comparison of the predictions of all the obstacles geometries shows that the influence of the cross-flow are greater, as the mean cross-flow velocities are higher and at a peak in the plane of the obstacles (or between the holes) as in Figure 7 (i). For the obstacle walls of cross-flow, the deflection of the jet by the higher cross-flow velocity over the walls is quite high, which is expected to generate higher turbulence hence good cooling. In the downstream cooling, the deflected jets impinges on the upstream face of the walls and this will produce good cooling there, as shown by Figure 7 (ii) and predicted using the normalized temperature (or thermal gradient) T^* of Equation 2. Figure 6 (i) and ii reveals that the co-flow geometries have insignificant jet deflections as the flow in the downstream holes is relatively close to the upstream one, as Figure 6ii shows, this flow is quite higher at downstream than for the cross-flow geometry. Figure 7 (ii) shows that lowest thermal gradients exist in the rectangular pin obstacles, this expected as the gap blockage is the minimum.

$$V_j = \frac{G}{\rho A} = \frac{4G}{\pi\rho}\left(\frac{X}{D}\right)^2 = C_d\left(2RT\frac{\Delta P}{P}\right)^{0.5} \quad (1)$$

$$T^* = \frac{(T - T_\infty)}{(T_w - T_\infty)} \quad (2)$$

3.2 Predicted Axial Pressure Loss Profiles

The cross-flow obstacles create a blockage to the cross-flow downstream the impingement gap (Abdul Husain and Andrews, 1991, Andrews *et al.*, 2003), as in Table 2. This increases the pressure loss shown in Equation 1 due to the cross-flow as Figure 8a show to leads to an increased flow-maldistribution between the impingement holes for all the cross-flow configurations, which block the downstream cross-flow. Figure 7 shows that the co-flow obstacles that have the minimum blockage to the cross-flow have a flow-maldistribution similar to the smooth wall predictions of El-jummah et al. (2014b, 2013a), which have similar relative pressure loss ΔP/P as in Figure 8a. The downstream impingement gap cross-flow over the obstalces leads to higher ΔP/P as shown in Figure 8a. The increased flow-maldistribution with obstacles also creates a lower pressure loss across the leading

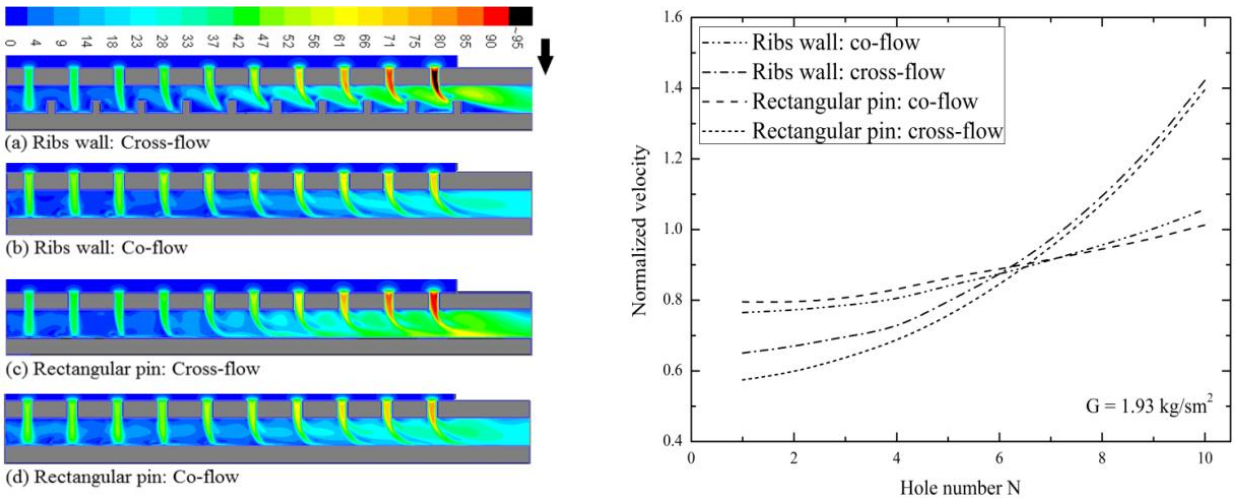

(i) Velocity magnitude (m/s) in the plane of the holes (ii) Flow-maldistribution in the impingement jet holes

Figure 6: Influence of flow aerodynamics with obstacles in the jet holes for G of 1.93 kg/sm^2

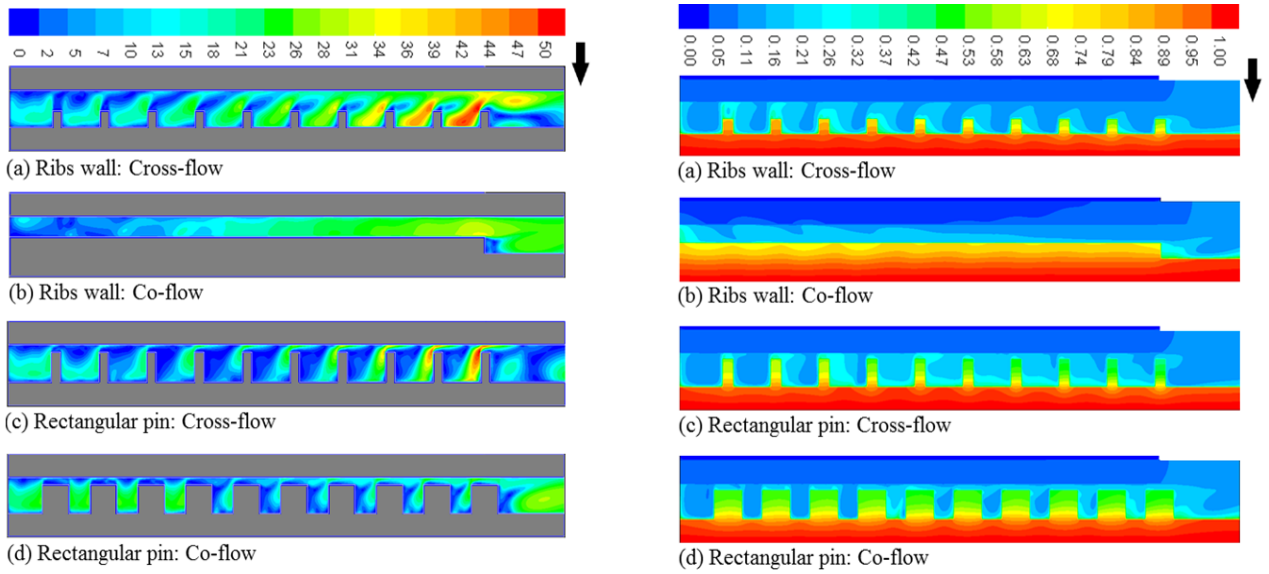

(i) Velocity magnitude (m/s) in the obstacles plane (ii) Normalized temperature in the obstacles plane

Figure 7: Impingement gap contours of flow and heat in the fluid and walls for G of 1.93 kg/sm^2

The holes in the gap, which is the effect that gives rise to the increased flow-maldistributoin in Figure 7 (ii). Figure 8a shows that the cross-flow obstacle geometries are predicted to have higher pressure loss than the co-flow geometries, which was expected as there was increased cross-flow velocity in the gap with blockage. However, the reduced ΔP/P for co-flow with ribs was unexpected, it appears that as the rib prevents the impingement flow of adjacent jets in the transverse direction, it changes the reverse flow jet in a way that reduces its impact on the cross-flow ΔP/P. This pressure loss will also be seen to influence the heat transfer that will be predicted using Equation 3.

$$h = \frac{q''}{(T_s - T_\infty)} \tag{3}$$

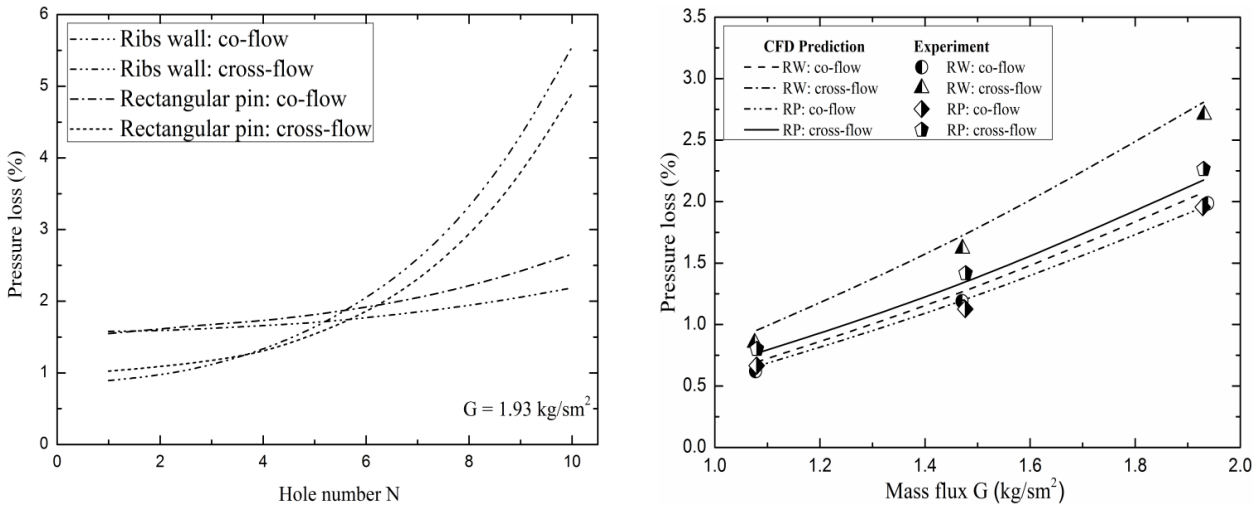

(a) Impingement hole outlet pressure loss (b) Impingement gap exit pressure loss for all G

Figure 8 Effects of mass flux G in the impingement hole and gap exits aerodynamics

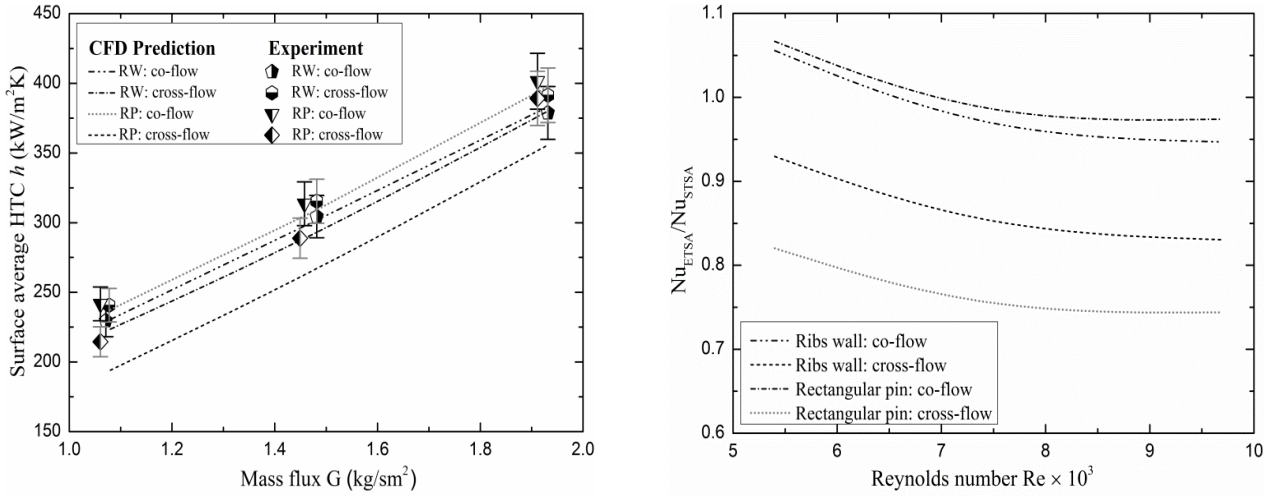

(a) Surface average HTC validation (b) Nusselt number over smooth average one

Figure 9: Comparison of predicted and measured/CFD heat transfer for the range of flow values

3.3 Validation of CFD Predictions

Figure 8b compares the measured (Abdul Husain and Andrews, 1991, Andrews *et al.*, 2003, 2006) and predicted pressure loss, from the air feed plenum static pressure to the impingement gap exit static pressure well downstream of the last obstacle, which is the overall wall relative pressure loss ΔP/P. The ΔP/P predictions for range of G values that were shown in Table 4 for the co-flow obstacles and that for the rectangular pin cross-flow gave excellent agreement with the measurements, but the ribs wall cross-flow obstacle shows slightly higher predicted pressure loss. The reason for this was that in cross-flow continuous ribs, the distance downstream of the last obstacle for the flow to have recovered the dynamic pressure due to flow acceleration was longer than the computational domain. These predicted and measured pressure loss agreements indicate that the aerodynamics was adequately modelled. The two continuous rib designs would be expected to increase the pressure loss as they have a 45% blockage (Table 2 based on H design) of the cross-flow and both force the cross-flow to deflect towards the impingement jet wall. The full height of the impingement gap is available for the downstream cross-flow in these designs, whereas the continuous ribs force this cross-flow to separate from the surface, which appears to be the key reason for the increased in pressure loss for the continuous ribs in cross-flow.

It has previously been shown that the present CFD procedures, predicted the measured smooth wall impingement heat transfer results (El-Jummah *et al.*, 2014b, 2013a, 2013b, c). The predictions of the target surface average HTC *h* on the influence of obstacle walls are compared with the measured HTC (Abdul Husain and Andrews, 1991, Andrews *et al.*, 2003, 2006) in Figure 9a and were based on Equation 3. All the predictions for the surface averaged HTC are within 12 % of the measurements at all G, as generally any error is an under prediction. For the continuous rib with co-flow, the agreement was perfect with no significant error at any G. For the rib wall in cross-flow, the predictions were 6 % low at low G and 3 % low at high G. For the rectangular pin fin in co-flow the predictions were also in good agreement at all G. For the rectangular pin fins in cross-flow the predictions were 8 % low at high G and 12 % low at low G. The more complex is the interactions of cross-flow with the obstacle, the higher the error that was found. However, these predictions for most of the geometries are sufficiently close to the measured ± 10 % error (El-Jummah *et al.*, 2014b) bars in Figure 9a to have confidence that surface averaged *h* were reliably

predicted. The predicted enhanced target surface averaged Nusselt number Nu variations based on Equation 4, averaged over the smooth target average Nusselt number Nu (El-Jummah *et al.*, 2014b) as a function of Reynolds number Re is shown in Figure 9b. The co-flow obstacles predicted the average Nu to be above that of the smooth target walls, while cross-flow obstacles are below. This indicates that most of the cooling has been taking away by the cross-flow obstacle walls.

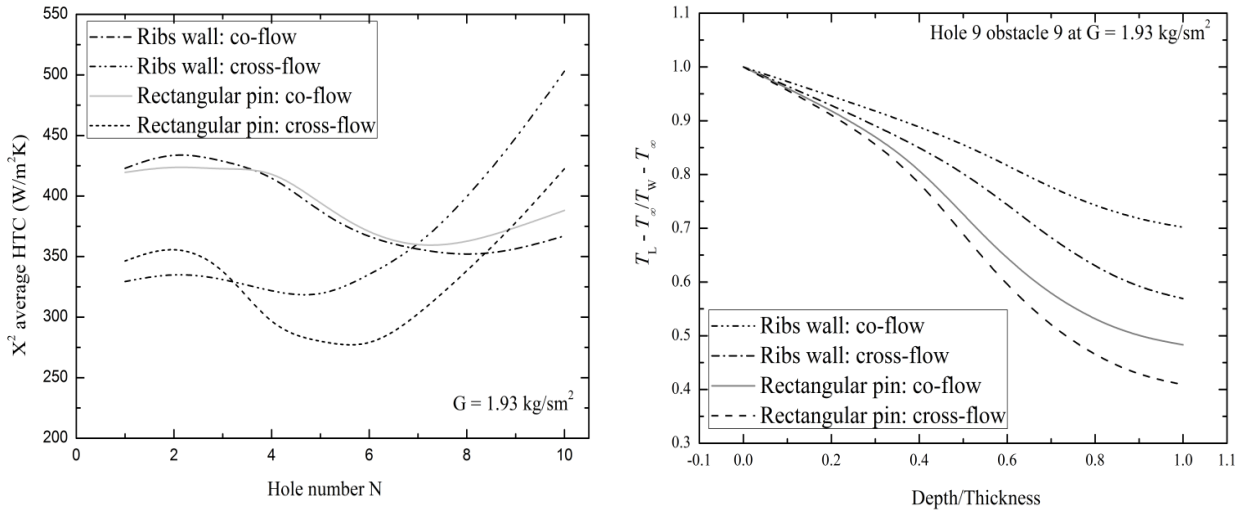

(a) Target surface X^2 average HTC h (b) Wall normalized thermal gradients

Figure 10: Predicted conjugate heat transfer of the obstacle walls for range of G values

$$Nu = \frac{hD}{k_f} \tag{4}$$

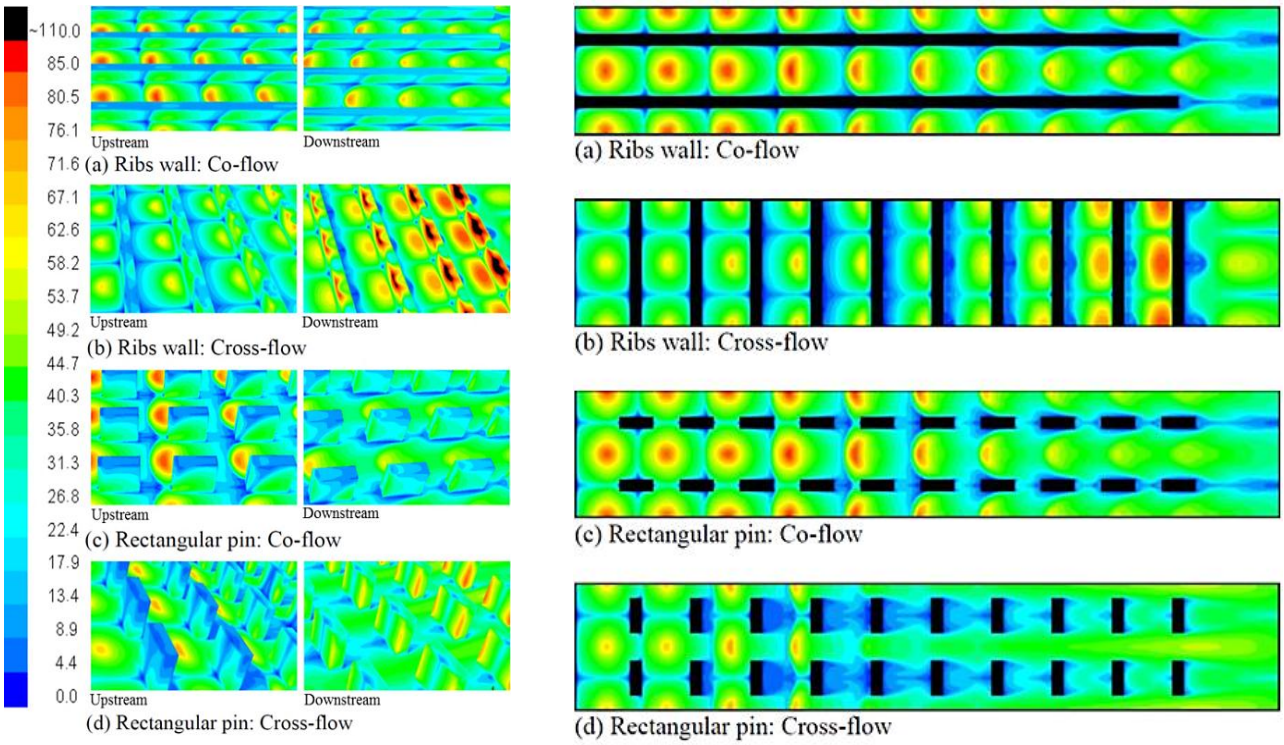

Figure 11: Contours of Nusselt number on the target wall with the obstacles for G of 1.93 kg/sm^2

The above assertion for the cross-flow obstacles, are further shown in Figure 10a which is the predicted locally X^2 averaged *h* in the absences of the obstacles. It shows that the downstream X^2 averaged *h* cooling of the cross-flow geometries is insignificant as compared to the co-flow, whereby at the upstream last holes the cooling is above the later. This must be the reason for the surface average better cooling shown in Figure 9b that the co-flow Nu predictions are above cross-flow ones. The thermal gradients through the combined target and obstacles walls for the obstacles at the hole 9 position are predicted in Figure 10b, whereby the smooth wall predictions are shown for comparison. The lowest thermal gradients T^* are predicted in Figure 10b to be in the region close to the jet plates. The ribs obstacles gave higher thermal gradients, with the pin fins having the greatest gradients, which was based on the impingement gap blockage as pins have the highest.

3.4 Surface Distribution of Nusselt Number

Figure 11 shows the CHT CFD predicted surface distribution of Nusselt number Nu on the enhanced target surface, predicted using Equation 4, where left side is Nu with the obstacles and right side without. The Nu surface distribution is very similar to that of the TKE in Figure 12 (i) which gave rise to Figure 12 (ii). Figure 11 shows that most the cooling Nu are either between the obstacles typical of the co-flow or on the obstacles for the cross-flow and lower Nu values are on the upstream obstacles. Any enhancement of heat transfer has to come from the heat transfer to the rib or pin fin surfaces, which is not shown in Figure 11. The quite poor Nu distribution for the rectangular pin on the target surface is partially compensated for by the heat transfer on the cross-flow obstacle surfaces, which extract heat from the target surface by conduction. The heat transfer to the obstacle surfaces was shown in Figure 9b, which shows the high heat transfer on the rib and rectangular pin fins surfaces in the downstream part of the flow, where the cross-flow deflects the jets strongly onto the rib in cross-flow surface.

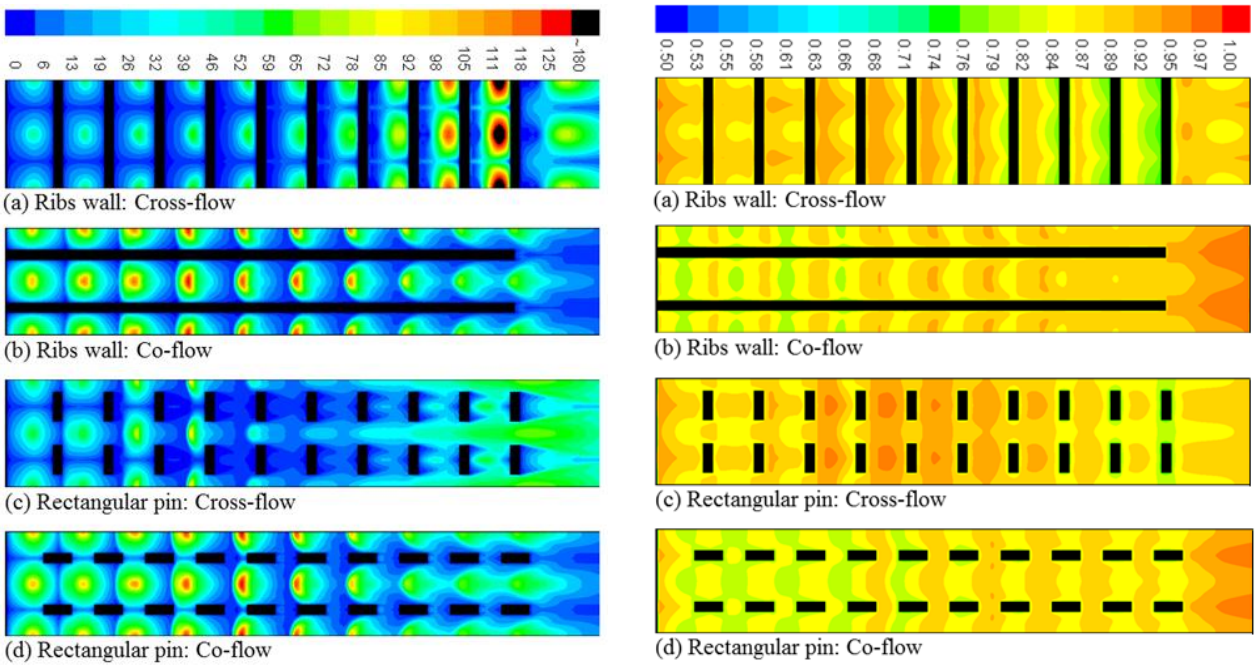

(i) Turbulence kinetic energy for G of 1.93 kg/sm^2 (ii) Normalized temperature for G of 1.93 kg/sm^2

Figure 12: Enhanced target surface distribution of TKE and T^* showing the influence of obstacles

3.5 Temperature Gradients through Enhanced Walls

Figure (ii) shows the enhanced target surface distribution of normalised temperature T^* of all the obstacle walls, found using Equation 2. The region of the lowest distributions of T^* indicates the region with the higher HTC or Nu (based on Equations 3 or 4). Fig) show that the lowest surface temperatures and temperature distribution were for the upstream co-flow region, this is the region of the highest TKE shown in Figure 12 (i). This was due to the reduced impingement cooling by the obstacle walls, which normally is unexpected as the walls takes away most of the cooling (Figure 11 left hand side). The configuration for the downstream cross-flow rib-wall obstacle showed very good cooling, but the implication could be inadequate overall cooling and increased flow-maldistribution as in Figure 6ii. This affects the upstream thermal gradient as in Figure 12ii (a) as the influence of TKE is very much pronounced at that region as Figure 12 (ia) show and is the region of the pick turbulence. Figure 7 (iic and d), shows that the better cooled obstacles are that for the high blockage wall, as also shown by Figure 11 (c and d).

4. Conclusions

The CHT CFD predictions of the enhanced impingement heat transfer for G of 1.08, 1.48 and 1.93 kg/sm^2 at fixed X/D of 4.66 and Z/D of 3.06 showed good agreement with the experimental surface average HTC. The predictions of the pressure loss were in very good agreement with the measurements, indicating that the aerodynamics were adequately predicted.

The predictions showed that it was difficult to enhance the smooth wall impingement heat transfer and that obstacles could deteriorate the heat transfer. The main effect of the obstacles was to enhance the heat transfer to the impingement jet wall and decrease it to the target wall. A small increase in the overall surface average heat transfer was predicted for the co-flow configuration with ribs.

The geometrical model design and the predicted results for the enhanced cooling heat transfer in gas turbine system showed that design optimisation using CHT CFD tool could be reliable.

References

Abdul Husain, RAA. and Andrews, GE. 1991. Enhanced Full Coverage Impingement Heat Transfer With Obstacle in the Gap. Proceedings of the ASME International Gas Turbine & Aeroengine Congress & Exposition, 91-GT-346: 1 - 12.

Andrews, GE., Abdul Husain, RAA. and Mkpadi, MC. 2003. Enhanced Impingement Heat Transfer: Comparison of Co-Flow and Cross-flow with Rib Turbulators. Proceedings of the GTSJ International Gas Turbine Congress, IGTC TS-075: 1 - 8.

Andrews, GE., Abdul Husain, RAA. and Mkpadi, MC. 2006. Enhanced Impingement Heat Transfer: The Influence of Impingement X/D for Interrupted Rib Obstacles (Rectangular Pin Fins). TransASME Turbomachinery, 128**:** 321 - 331.

Andrews, GE. and Hussain, CI. 1984. Impingement Cooling of Gas Turbine Components. High Temperature Technology, 2 (2)**:** 99 - 106.

Andrews, GE. and Hussain, CI. 1987. Full Coverage Impingement Heat Transfer: The Influence of Cross-Flow. AIAA/SAE/ASME/ASEE 23rd Joint Propulsion Conference, AIAA-87-2010**:** 1 - 9.

Azad, GMS., Huang, Y. and Han, J. 2002. Jet Impingement Heat Transfer on Pinned Surfaces Using a Transient Liquid Crystal Technique. International Journal of Rotating Machinery, 8 (3)**:** 161 - 173.

Bailey, JC. and Bunker, RS. 2002. Local Heat Transfer and Flow Distributions for Impinging Jet Arrays of Dence and Sparse Extent. Proceedings of the ASME Turbo Expo, GT-30473**:** 1 - 10.

Bunker, RS. 2008. The Effects of Manufacturing Tolerances on Gas Turbine Cooling. Proceedings of the ASME Turbo Expo, GT-50124**:** 1 - 16.

Chung, H., Park, SJ., Park, S., Choi, SM., Cho, HH. and Rhee, DH. 2014. Augmentated Heat Transfer for a Angled Rib With Intersecting Rib in Rectangular Channels of Different Aspect Ratios. Proceedings of the ASME Turbo Expo, GT-26924:1 - 13.

El-Jummah, AM., Abdul Hussain, RAA., Andrews, GE. and Staggs, JEJ. 2014a. Conjugate Heat Transfer CFD Predictions of Impingement Heat Transfer: Influence of the Number of Holes for a Constant Pitch to Diameter Ratio X/D. Proceedings of the ASME Gas Turbine Conference, GT-25268**:** 1 - 14.

El-Jummah, AM., Abdul Hussain, RAA., Andrews, GE. and Staggs, JEJ. 2014b. Conjugate Heat Transfer Computational Fluid Dynamic Predictions of Impingement Heat Transfer: The Influence of Hole Pitch to Diameter Ratio X/D at Constant Impingement Gap Z. TransASME Turbomachinery, 136 (12)**:** 1 - 16.

El-Jummah, AM., Andrews, GE. and Staggs, JEJ. 2015. CHT/CFD Predictions of Impingement Cooling With Four Sided Flow Exit. Proceedings of the ASME Turbo Expo, GT-42256: 1 - 12.

El-Jummah, AM., Andrews, GE. and Staggs, JEJ. 2016. Impingement Jet Cooling with Ribs and Pin Fin Obstacles in Co-flow Configurations: Conjugate Heat Transfer Computational Fluid Dynamic Predictions. Proceedings of the ASME Turbo Expo: Turbomachinery Technical Conference & Exposition, GT- 57021**:** 1 - 15.

El-Jummah, AM, Abdul Hussain, RAA., Andrews, GE. and Staggs, JEJ. 2013a. Conjugate Heat Transfer CFD Predictions of the Surface Averaged Impingement Heat Transfer Coefficients for Impingement Cooling with Backside Cross-flow. Proceedings of the ASME IMECE Conference, IMECE-63580**:** 1 - 14.

El-Jummah, AM. Andrews, GE and Staggs, JEJ 2013b. Conjugate Heat Transfer CFD Predictions of Impingement Jet Array Flat Wall Cooling Aerodynamics with Single Sided Flow Exit. Proceedings of the ASME Turbo Expo Conference, GT-95343**:** 1 - 12.

El-Jummah, AM. Andrews, GE. and Staggs, JEJ. 2013c. Conjugate Heat Transfer CFD Predictions of the Influence of the Impingement Gap on the Effect of Cross-Flow. Proceedings of the ASME Heat Transfer Conference, HT-17180**:** 1 - 12.

Friedman, SJ. and Mueller, AC. 1951. Heat Transfer to flat surfaces. Proceedings of the IMechE: General Discussions on Heat Transfer**,** 138 - 142.

Hoefler, F., Schueren, S., Wolfersdorf, J. and Naik, S. 2012. Heat Transfer Characteristics of an Oblique Jet Impingement Configuration in a Passage With Ribbed Surfaces. TransASME Turbomachinery, 134**:** 1 - 9.

Kercher D. M. and Tabakoff W. 1970. Heat Transfer by a Square Array of Round Air Jets Impinging Perpendicular to a Flat Surface Including Effect of Spent Air. TransASME Power Engineering**:** 73 - 82.

Ligrani, PM. 2013. Review Article: Heat Transfer Augmentation Technologies for Internal Cooling of Turbine Components of Gas Turbine Engines. Journal of Rotating Machinery, ID. 275653**:** 1 - 32.

Ligrani, PM., Oliveira, MM. and Blaskovich, T. 2003. Comparison of Heat Transfer Augmentation Techniques. AIAA Journal, 41 (3)**:** 337 - 362.

Rundstrom, D. and Moshfegh, B. 2008. Investigation of Heat Transfer and Pressure Drop of an Impinging Jet in a Cross-Flow Cooling of Heated Cube. TransASME Heat Transfer, 130**:** 1 - 13.

Sharif, MAR. and Mothe, KK. 2009. Evaluation of Turbulent Models in the Prediction of Heat Transfer Due to Slot-Jet Impingement on Plane Concave Surfaces. Numerical Heat Transfer, Part B, 55**:** 273 - 294.

Sharif, MAR. and Mothe, KK. 2010. Parametric Study of Turbulent Slot-Jet Impingement Heat transfer from Concave Cylindrical Surfaces. International Journal of Thermal Sciences, 49**:** 428 - 442.

Shizuya, M. and Kawaike, K. 1987. Experimental Investigation of Blade Internal Cooling Methods Using Ribs and Fins. Proceedings GTSJ International Gas Turbine Congress, IGTC-65**:** 159 - 166.

Spring, S., Xing, Y. and Weigand, B. 2012. Experimental and Numerical Study of Heat Transfer from Arrays of Impinging Jets With Surface Ribs. ASME Journal of Heat Transfer, 134**:** 1 - 11.

Tapinlis, O., Choi, M., Gillespie, DRH., Lewis, LV. and Ciccomascolo, C. 2014. The Effect of Impingement Jet Heat Transfer on Casing Contraction in a Turbine Case Cooling System. Proceedings of the ASME Turbo Expo, GT-26749**:** 1 - 11.

Taslim, ME. and Fong, MKH. 2011. Experimental and Numerical Crossover Jet Impingement in a Rib-Roughened Airfoil Trailing-Edge Cooling Channel. Proceedings of the ASME Turbo Expo, GT-45995**:** 1 - 12.

Taslim, ME., Pan, Y. and Spring, SD. 2001. An Experimental Study of Impingement on Roughened Airfoil Leading-Edge Walls With Film Holes. TransASME Turbomachinery, 123**:** 766 - 773.

Trabold, TA. and Obot, NT. 1987. Impingement Heat Transfer Within Arrays of Circular Jets: Part II - Efects of Cross-Flow in the Presence of Roughness Elements. TransASME Turbomachinery, 109**:** 594 - 601.

Wang, Z., Ireland, PT., Kohler, ST. and Chew, JW. 1998. Heat Transfer Measurements to a Gas Turbine Cooling Passage With Inclined Ribs. TransASME Turbomachinery, 120**:** 63 - 69.

Xie, Y., Li, P., Lan, J. and Zhang, D. 2013. Flow and Heat Transfer Characteristics of Single Jet Impinging on Dimpled Surface. TransASME Heat Transfer, 135**:** 1 - 15.